6

# Ultrafast Fabrication of Metal Nanostructures Using Pulsed Laser Melting

Bo Cui
*Waterloo Institute for Nanotechnology (WIN)*
*University of Waterloo*
*Canada*

## 1. Introduction

Nanoimprint lithography (NIL) is a mechanical molding process. Two formats of NIL are commonly used: thermal NIL and UV-curing NIL. In thermal NIL, the resist is typically a thermoplastic or thermoset polymer that becomes soft at temperatures well above its glass transition temperature, thus it can be imprinted by a rigid mold. NIL has demonstrated low cost and high throughput patterning (Chou 1996, Schift 2008) with a high resolution of sub-5 nm (Austin 2004, Hua 2004). However, due to their very high melting temperature, direct patterning of metal or silicon using an NIL-like process is very challenging.

Previously, metal structure fabrication by transfer-printing or imprinting without melting has been demonstrated. For instance, Kim et al used a hard silicon mold to press into a metal film on a substrate with a high pressure of 290 MPa that fractured the metal film at the mold pattern edge; and they then peeled off the metal and transfer-printed it to another substrate, achieving sub-micrometer resolution (Kim 2000). Yu et al fabricated Ag metal electrodes for organic light emitting devices by transfer-printing with a polydimethylsiloxane (PDMS) stamp, which peels off the portion of the metal film that is in contact with the protruded PDMS patterns (Yu 2007). However, it has a low resolution of 13 µm and a low yield that depends on the peel direction. Buzzi et al, Pang et al and Hirai et al applied ultra-high pressure of several hundred MPa to directly imprint a solid metal at room temperature (Buzzi 2008, Pang 1998, Hirai 2003). Chen et al and Chuang et al used a mold having a sharp geometry to deform or imprint (penetrate) metal thin films (<50 nm) deposited on a soft polymer bottom layer at pressure of 10-20 MPa and temperature slightly lower than the glass transition temperature of the bottom polymer (Chen 2006, Chuang 2008). The above methods suffer from poor patterning resolution and are limited to ductile metals because, during the patterning, the metals are in the hard solid phase.

In this chapter, we present a method of direct patterning of metal or silicon nanostructures using a pulsed laser that can melt the metal or silicon. Like the aforementioned method, the most prominent feature of this technique is that it is a one-step patterning process – it replaces the steps of resist patterning in lithography, subsequent pattern transfer by etching or liftoff, and resist removal all by one single simple step. In addition, as molten metal or silicon has very low viscosity (on the same order as water), this technique can pattern them

within ~100 ns. It can also anneal the patterned metallic nanostructures. More importantly, the current method is not limited to ductile metals, and hard metals like nickel can be structured readily.
Various applications have been developed, and here we will present laser assisted direct imprint, wafer planarization, via-hole filling, transfer printing, and nano-tip formation. Other important applications using pulsed laser nanofabrication, such as self-perfection by liquefaction (SPEL) that removes nanostructure fabrication defects (notably line edge roughness) (Chou 2008, Xia 2010), and nano-channel fabrication using sealing by laser-melting (Xia 2008), will not be presented.

## 2. Fundamentals of laser-matter interaction

Fig. 1 illustrates schematically the laser-matter interaction at a wide range of power and/or energy density. The pulsed laser we used at the Nanostructure Laboratory, Princeton University, is a 308 nm XeCl excimer laser with pulse duration of 20 ns (FWHM), maximum output energy of 200 mJ per pulse, and power of 160 $MW/cm^2$ for a beam size of $(2.5 mm)^2$ if assuming a rectangular temporal pulse shape. With this laser, a power density of order of 10 $MW/cm^2$ is needed to melt a 200 nm-thick thin metal or semiconductor film on an insulator, whereas order 100 $MW/cm^2$ is necessary for substantial vaporization and/or plasma formation. In the following sections, three topics will be covered in some detail: light absorption by metals and semiconductors, transient heat transfer and temperature distribution, and vaporization, plasma formation and plasma propagation.

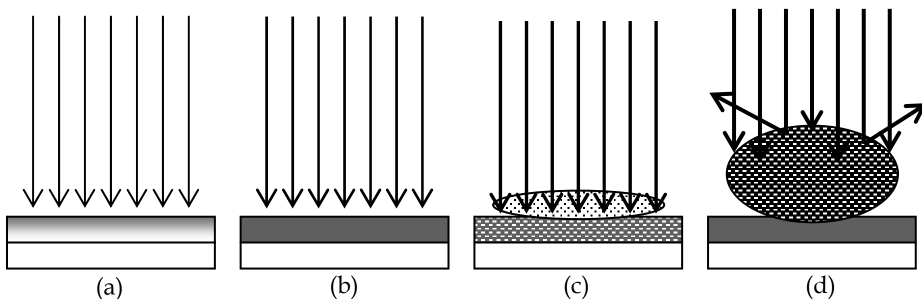


Fig. 1. Schematic laser-material interaction. (a) Absorption and heating. (b) Melting and flowing. (c) Vaporization. (d) Plasma formation in front of the target. Under certain conditions the plasma can detach from the target and propagate toward the laser beam.

### 2.1 Absorption of laser light

Laser light must first be absorbed in order to cause any lasting effect on a material. Electromagnetic radiation with a wavelength between UV and IR interacts exclusively with electrons, as atoms are too heavy to respond significantly to the high frequencies ($>10^{13}$ Hz) involved. Therefore, the optical properties of matter are determined by the energy states of its valence electrons (bound or free). Generally, bound electrons can only weakly respond to the external electromagnetic wave and merely affect its phase velocity. Free electrons are able to be accelerated, i.e., to extract energy from the field. However, since the external field is periodically

changing, the oscillating electrons re-radiate their kinetic energy, unless they undergo frequent collisions with the atoms – in this case energy is transmitted to the lattice (absorbed) and the external field is weakened. Re-radiation of the energy is the cause of reflection.
For absorbing media the refractive index is a complex number with the form n=n+ik. The reflectivity at normal incidence is (n=1 for air or vacuum)

$$R = \frac{(n-1)^2 + k^2}{(n+1)^2 + k^2} \tag{1}$$

The emissivity, or the fraction of incident radiation absorbed, is then

$$\varepsilon \equiv 1 - R = \frac{4n}{(n+1)^2 + k^2} \tag{2}$$

The absorption coefficient is defined as

$$\alpha \equiv -\frac{1}{I}\frac{dI}{dz} = \frac{4\pi k}{\lambda} \tag{3}$$

where I is the intensity of the incident light (also termed irradiance, in $W/cm^2$). The inverse of $\alpha$ is referred as the absorption length. For normal incidence the power density (in $W/cm^3$) deposited at depth z is

$$\Phi(z) = I(1-R)\alpha e^{-\alpha \cdot z} \tag{4}$$

### 2.1.1 Low light intensity and temperature regime

Both n and k (thus $\alpha$) are generally functions of wavelength and temperature. For a semiconductor such as silicon (see Fig. 2 (a)), the absorption coefficient $\alpha$ increases with decreasing wavelength $\lambda$ gradually near its indirect band-gap at 1.1 eV (1.13 μm), but increases rather abruptly near its direct band-gap at 3.4 eV (0.36 μm) because no phonons are involved for direct transition. At photon energies significantly exceeding $E_g$, the optical response of semiconductors tends towards that of metals.
Fig. 2 (b) depicts the light-coupling parameters for Al and Au. Metals, due to their large density of free electrons close to the Fermi level, have large absorption coefficients (corresponding to absorption lengths $\alpha^{-1}$ around only 10 nm) over the whole spectrum. Their reflectivity is more difficult to determine than that of semiconductors. Generally, their reflectivity is high above a certain critical wavelength that is related to its electron plasma frequency $\omega_p$ given by $\sqrt{(4\pi Ne^2/m_e)} \propto \sqrt{N}$, where N is electron density and $m_e$ is electron mass. Below the critical wavelength, which is in the UV or visible part of the spectrum, R decreases sharply. For Au and Cu, the plasma frequency is reduced (which causes their yellow color) by transition from d-band states.

### 2.1.2 High light intensity and/or temperature regime

At higher light intensities and/or higher temperatures, the optical properties can be modified by three mechanisms: lattice heating, free carrier generation (for semiconductors only) and excitation. At elevated temperatures, more phonons are present, leading to an increase of lattice-carrier collision. As a result, the reflectivity of most metals decreases with increasing temperature, and this effect makes metals susceptible to thermal runaway.

For semiconductors like silicon, a large number of free carriers can be generated not only by thermal excitation at high temperature and further facilitated by the band-gap narrowing, but also by photons at a rate of $I\sigma/h\nu$ (I is light intensity, $\sigma$ is the absorption cross section) when $h\nu > E_g$. Fig. 3 depicts the energy diagram of the electrons (holes have similar diagram) under intense irradiation such that the carrier generation rate exceeds that of carrier relaxation rate. Due to free carrier generation, the carrier density and thus the absorption coefficient $\alpha$ of semiconductors increase strongly as a function of light intensity. The effect of free carriers on the optical properties is to reduce the real part and to increase the imaginary part of **n**. As a result, free carrier generation tends to decrease the reflectance for $\omega_p < \omega$ (now $\omega_p \propto \sqrt{N}$ is a variable depending on light intensity, while $\omega$ is fixed). Only for carrier density N large enough that $\omega_p > \omega$ does the reflectance begin to increase with the light intensity towards unity by further increasing $\omega_p$. Such a rich variation of reflectivity on light intensity and time has been observed for crystalline Si irradiated by red 90 fs pulses (Shank 1983).

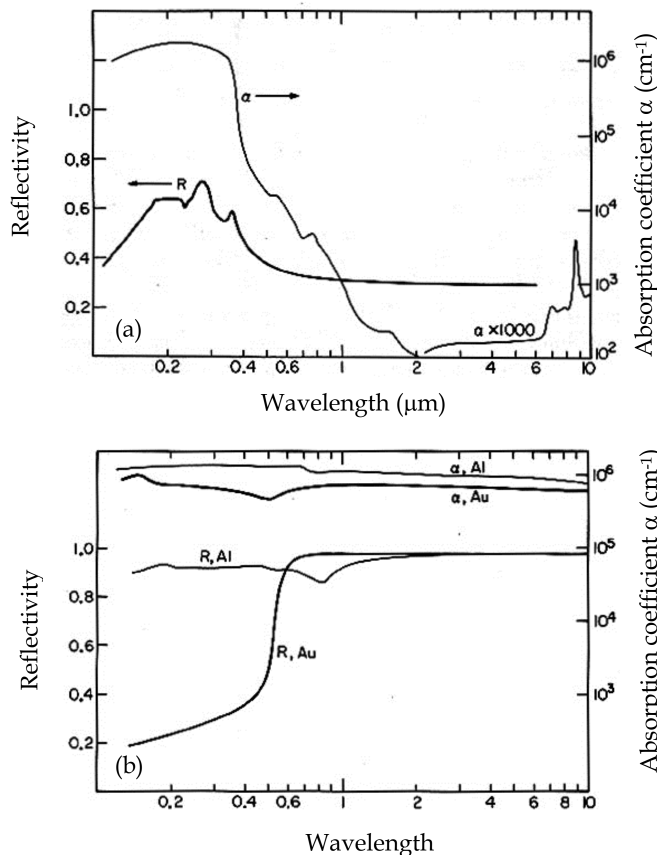


Fig. 2. Reflection and absorption coefficient as a function of wavelength for (a) silicon, and (b) Al and Au. The critical wavelength of Al is below 100 nm, so its reflectivity is close to 1 over the data range in the figure. (from Allmen, 1995)

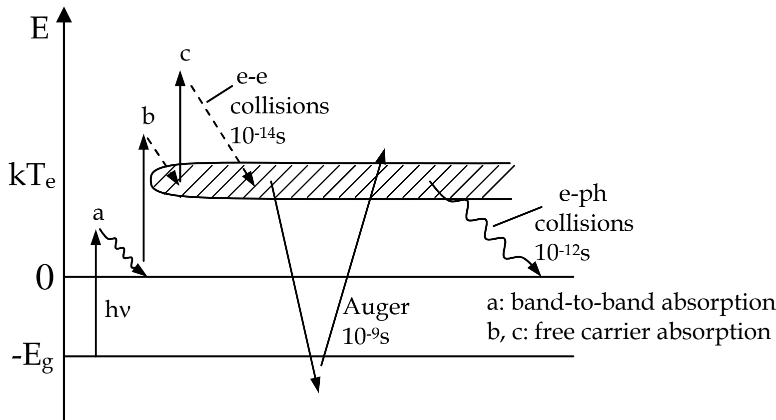


Fig. 3. Schematic energy diagram of the electrons in a semiconductor under intense irradiation. The electron temperature $T_e$ is higher than the lattice temperature. The shaded area depicts electron plasma. (adapted from Poate 1982)

At sufficiently high light intensity, the rate of energy gain by carriers exceeds the rate of energy loss to the lattice. The result is a splitting up of carrier and lattice temperatures (see Fig. 3), and the carriers behave collectively, i.e., according to the equations governing a plasma (but this plasma behavior is not to be confused with the generation of actual plasma shown in Fig. 1(d); the plasma here is just a large number of electrons inside the conduction band of the semiconductor). The plasma may be regarded as an independent system which absorbs light and exchanges energy with the lattice. As far as coupling is concerned, the effect of the plasma is ultimately to limit the rate of local energy deposition by increasing R at high carrier density such that $\omega_p > \omega$, and by diffusing away the hot carriers from the absorbing surface to the material underneath, which effectively increases the heated volume.

Finally, Si and Ge become metallic (silicon's electrical conductivity is 30 times higher) upon melting due to bandgap collapsing, leading to a strong increase in both $\alpha$ and R.

## 2.2 Heating and melting by laser

Heating in an irradiated sample is a consequence of the balance between the deposited energy, governed by optical parameters of the sample and characteristics of the laser pulse, and the heat diffusion, determined by thermal parameters and the pulse duration. Strictly speaking, as discussed in the previous section, the primary product of absorbed laser light is not heat but the carriers' excess energy. But for simplicity, and because the our laser pulse has a relatively long duration of 20 ns, it can be assumed that the overall energy relaxation time $\tau_E$ is negligible compared to the pulse duration ($\tau_E$~$10^{-13}$s for metals, ~$10^{-12}$ – $10^{-9}$s for semiconductors). With this assumption, a simple estimate of the temperature rise is possible for two limiting cases in which the optical absorption depth is small compared with the thermal diffusion length during the pulse (i.e. $\alpha^{-1} \ll \delta \equiv 2\sqrt{Dt}$.), or vice versa. However, for many practical cases, complex analytical or numerical evaluations must be performed. In particular, if phase transitions occur during the irradiation, only numerical solutions are available.

In the current experiment with XeCl excimer laser irradiation of semiconductors or metals, the absorption depth is much smaller than the thermal diffusion length. However, great complexities come from the multi-layered substrate/mold system bearing on its surface subwavelength patterns. Moreover, melting or even boiling was always seen in these experiments. And the parameters such as reflectivity, absorption coefficient, thermal conductivity and specific heat, are all strong functions of temperature. As a consequence, even numerical calculation will be very difficult unless significant simplifying assumptions are made. Therefore, in this section, only a rough estimation of the temperature distribution will be derived.

First, consider the case when phase change is absent. The excimer laser has a 2.5 mm beam size, which is many orders larger than the film thickness, so the heating and cooling can be approximated as a one-dimensional problem governed by the following equation:

$$\frac{\partial T}{\partial t} = \frac{\Phi(z,t)}{\rho C_p} + \frac{1}{\rho C_p}\frac{\partial}{\partial z}\left(\kappa \frac{\partial T}{\partial z}\right) \tag{5}$$

where $\Phi(z,t)$ is given by Eq. 4 that represents the source term, and $\rho$, $C_p$ and $\kappa$ are the density, specific heat and thermal conductivity, respectively. This equation can be solved analytically under the following assumptions: no temperature dependence of all optical and thermal parameters, rectangular temporal pulse shape of duration $t_p$ and intensity $I_0$ (the actual pulse shape is close to Gaussian), very small absorption length ($\alpha^{-1} << \delta$), and infinite sample thickness. The temperature distribution during and after the pulse is described by (Allmen 1995)

$$T(z,t) = \frac{2I_0(1-R)}{\kappa}\sqrt{Dt}\, ierfc[z/2\sqrt{Dt}] - [t > t_p]\sqrt{D(t-t_p)}\, ierfc[z/2\sqrt{D(t-t_p)}] \tag{6}$$

$$ierfc(x) = \int_x^\infty erfc(x')dx' \text{ and } erfc(x) = \frac{2}{\sqrt{\pi}}\int_x^\infty e^{-t^2}dt \tag{6'}$$

where thermal diffusivity $D \equiv \kappa/\rho C_p$ and the symbol $[t>t_p]$ equals one if $t>t_p$ and zero otherwise. The characteristic thermal diffusion length within time t is defined as $\delta \equiv 2\sqrt{Dt}$. Eq. 6 is visualized in Fig. 4, which suggests the maximum temperature at $z=\delta=2\sqrt{Dt_p}$ is about 1/5 that of peak surface temperature and it is reached at about $t=2t_p$. The surface temperature at the end of the pulse is

$$T(0,t_p) = \frac{2I_0(1-R)}{\kappa}\sqrt{Dt_p/\pi} \propto \sqrt{t_p} \tag{7}$$

On the other hand, for metal or semiconductor film sandwiched between the thermal insulating mold and substrate, if the film thickness h is far less than $\delta$, a more uniform temperature distribution is expected at the end of the pulse, and can be approximated by

$$T(z,t_p) = \frac{I_0(1-R)t_p}{C_p \rho h} \propto t_p \tag{8}$$

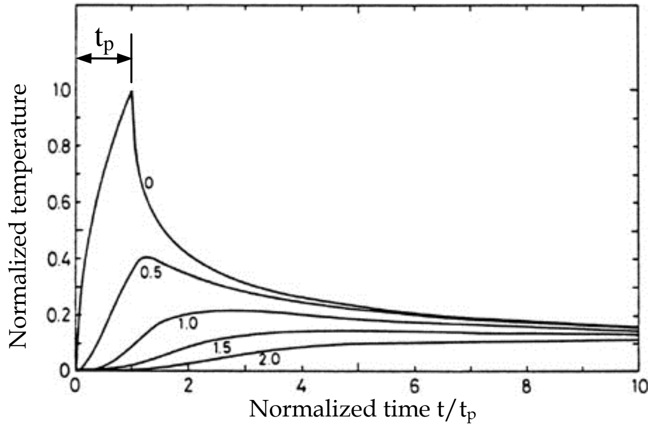


Fig. 4. Normalized temperature as a function of normalized time $t/t_p$ at various depths $z/\delta$ ($\delta=2\sqrt{Dt_p}$, $t_p$ is pulse duration) for a pulse of rectangular temporal shape, according to Eq. 6. Temperature is normalized to the surface temperature at the end of the pulse. (adapted from Allmen 1995)

Next, consider the case when the film is melted. The melting starts from the sample surface and propagates inside the sample until a maximum molten thickness is reached some time after the end of the pulse. The time period of melting depends on the energy density of the pulse and thermal properties of the material, and can be much longer than the pulse duration $t_p$. Fig. 5 sketches the temperature distribution and molten layer thickness variation with time. The latent heat $\Delta H_{sl}$ (the subscript "sl" denotes solid-liquid) for melting Al, Au, Cu, Ni and W ranges from 1/3 to 1/2 that of the energy needed to heat the materials from 300K to its melting temperature ($\Delta H_{300K\rightarrow Tsl}$), but for crystalline silicon the latent heat is 40% higher than its $\Delta H_{300K\rightarrow Tsl}$. Therefore, the film temperature is "pinned" near $T_{sl}$ to a larger degree for silicon than for those metals. During re-solidification, the velocity of the liquid-solid interface is determined by the rate of heat extraction from the interface into the bulk, and is given by

$$v = \frac{\kappa}{\Delta H_{sl}\rho}\left(\frac{\partial T}{\partial z}\right)_i \tag{9}$$

where $(\partial T/\partial z)_i$ is the temperature gradient just behind the interface, which is typically on the order of 1 K/nm. The resulting velocity is then on the order of several meters per second for silicon, and several tens of meters per second for metals.

## 2.3 Evaporation, plasma formation and plasma propagation

### 2.3.1 Evaporation and plasma formation

Due to their very low absorption length, the process window of irradiance for melting metals or semiconductors without surface vaporization is actually very narrow. At slightly higher laser intensity, significant material vaporization is induced and a dense vapor plume is formed in front of the target, a phenomenon known as ablation. For the our laser with 20 ns pulse duration and for film thickness around 200 nm, vaporization occurs when

irradiance exceeds several tens of MW/cm². There are two distinct modes of vaporization from a liquid, namely volume vaporization or boiling, and surface vaporization. For strongly absorbing media, surface vaporization is always the case. Yet boiling would take place first for backside irradiation, where the film is deposited on a transparent support and the irradiation comes from the support side. Owing to the inverse Mott's metal-insulator transition, the neutral (not ionized) metal vapor is insulating and transparent to the laser light.

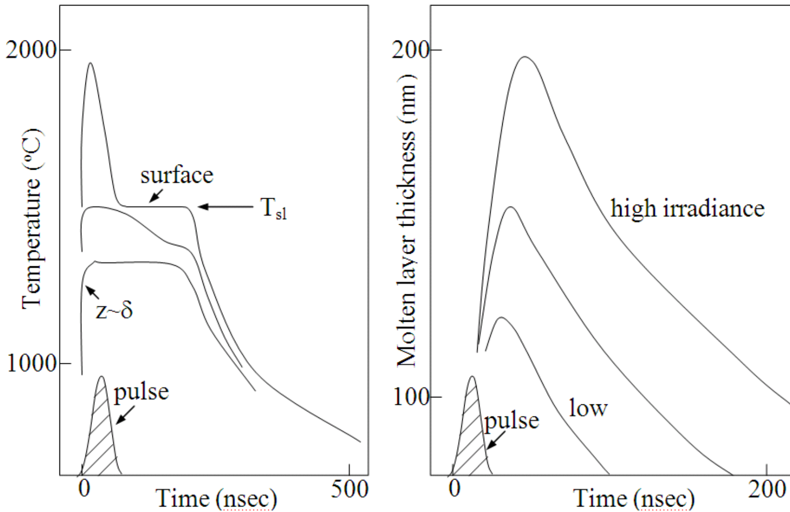


Fig. 5. Schematic time evolution of the temperature distribution (left) and the molten layer thickness (right) of a laser-irradiated sample. (sketch is partly based on the numerical simulation in Poate 1982 and Baeri 1979)

However, the regime of normal vaporization is relevant only for pulse durations longer than ~1 μs. For nanosecond pulses, unless the target is very thin and thus can be vaporized at low irradiance, the irradiance needed to substantially vaporize the target is often high enough to cause ionization and breakdown of vapor or gas (when ambient gas is present). The first breakdown mechanism is thermal ionization. The ratio of ions to neutrals for a gas in a local thermodynamic equilibrium is given by the Saha equation (Chrisey 1994):

$$\frac{n_i}{n_n} = 2.4 \times 10^{15} \frac{T^{3/2}}{n_i} e^{-E_I/kT} \tag{10}$$

where $n_i$ and $n_n$ are the ion and neutral densities and $E_I$ is the first ionization energy. Partially ionized gas absorbs light by thermally excited atoms as well as by electrons and ions (inverse-Bremsstrahlung absorption) (Hughes 1975). Light absorption further heats the vapor, which leads to even more ionization and absorption. The positive feedback favors the creation of plasma (substantially ionized vapor) in front of a vaporizing target. Thermal ionization turns on at lower irradiance for longer wavelength lasers because the optical absorption (∝αI) of the plasma increases strongly with increasing wavelength. The typical plasma temperature is ~10000 K, well above the boiling point of metals; and the associated

vapor pressure of the plasma is order of tens of atm. Above the cut-off electron density ($1.2\times10^{22}$ $cm^{-3}$ for 308 nm XeCl excimer laser) where $\omega_p>\omega$, the plasma behaves essentially like a metal with large absorption coefficient and high reflectivity. Below the cut-off density, the absorption coefficient of the plasma $\alpha_p$ decreases strongly with increasing temperature.
The second breakdown mechanism of the vapor or ambient gas is optical breakdown when the electrical field E of the light, given by $\sqrt{2I/\varepsilon_0 nc}$, reaches a critical point for avalanche ionization. The threshold irradiance $I_{th}$ is $10^9$−$10^{11}$W/cm$^2$ in *clean* air (no dust) at atmospheric pressure. In this case, initial ionization is achieved via multi-photon excitation since $h\nu<E_I$. However, for optical breakdown in front of a target, it was found that $I_{th}$ is about two to three orders of magnitude lower than if without a target. This is mainly due to the availability of primary electrons emitted from impurities absorbed on the target, which are evaporated and ionized far below the melting point of the target material, plus the temperature increase near a target. In laser processing, optical breakdown is the chief mechanism for plasma formation.
When ambient gas is present, three different laser intensity thresholds for plasma initiation should be distinguished: surface vaporization threshold $I_{vap}$, metal vapor plasma threshold $I_{i,m}$, and ambient gas plasma threshold $I_{i,g}$. Generally $I_{i,g}> I_{i,m}$ because metal atoms are easier to ionize than gas atoms. But gas breakdown usually occurs first for pulsed IR lasers because $I_{vap}$ is very high (so no metal vapor is produced for plasma formation) owing to metals' high reflectivity in the IR and rapid heat loss to the substrate. On the other hand, when a pulsed UV laser is used, metal vapor breakdown may happen first (Boulmer-Leborgne 1995).
With the formation of plasma, the plume strongly absorbs the laser light and shields the substrate from further irradiation. However, in addition to the shielding effect, there is an important energy transfer from the radiation emitted by the plasma to the surface and via heat conduction. Actually, plasma-enhanced coupling between laser and substrate often results, owing to the fact that the radiation emitted by the plasma is generally in the UV where most metals have low reflectivity.

### 2.3.2 Plasma propagation

At still higher irradiances depending on the wavelength, very thick (up to 10 cm) plasma can form that absorbs a significant fraction of the laser light, so laser-induced material vaporization at the target surface ceases. Then the plasma can decouple from the substrate and propagate toward the incident beam. Such plasma is often termed as laser-supported absorption wave, and its dynamic behavior is determined by the laser energy absorption within the plasma plume and the energy loss via heat conduction and plasma radiation. As the plasma leaves the target, it may fade out due to energy loss and become transparent again, which allows the substrate to be re-heated and re-vaporized that leads to a new cycle of plasma formation and propagation. If the plasma propagates with subsonic velocity, it is termed as laser-supported combustion wave (LSCW). The velocity of this wave increases with laser intensity. Plasma propagating at supersonic velocity is termed as laser-supported detonation wave (LSDW). In contrast to LSCW, LSDW is not confined to the vapor. Instead, through target surface-mediated optical breakdown, it can form in cold ambient gas even before the target has started to evaporate. Once ionized, the initial plasma tends to be strongly absorbing and can readily be sustained and propagated as an LSDW for laser irradiances of order $10^8$ W/cm$^2$. The temperature and pressure in an LSDW can reach $10^5$ K and $10^4$ atm, and due to its explosive nature, a shock wave (mechanical force) is driven into

both the ambient gas and the substrate material. For a more detailed discussion, refer to (Bäuerle 2000 and Allmen 1995).

## 3. Experimental setup

Fig. 6 shows the diagram of the setup. XeCl excimer laser with FWHM pulse duration of 20 ns was used to irradiate the samples. For 20 ns pulse duration, the characteristic thermal diffusion length ($\delta=2\sqrt{Dt_p}$) is calculated to be ~0.2 μm for $SiO_2$ and ~2 μm for metals and silicon. The maximum per pulse laser output energy is 200 mJ, yet 160 mJ was always set as maximum for more reproducible output fluence (energy divided by area, J/cm$^2$). The attenuator allows a transmission range of 10−90%. The incident laser beam has a square shape and its size, determined by the separation between the imaging doublet and the substrate, is chosen to be between 2 to 3 mm. With a 160 mJ pulse energy within 20 ns over the (2.5 mm)$^2$ beam area, the light intensity is calculated to be 130 MW/cm$^2$, high enough to cause vaporization and plasma formation in front of many metal targets. The sample stage is put either in air or in a vacuum chamber with vacuum better than 200 mTorr. The pressure between the mold and the substrate was applied by sandwiching them between two large press plates held by springs.

For laser assisted direct imprint (LADI), we used 200 nm period quartz (fused silica) grating mold that was duplicated by nanoimprint lithography, liftoff and reactive ion etching from a master mold, which was fabricated by interference lithography with uniform grating pattern over an entire 4″ wafer. The high purity quartz mold absorbs negligible laser energy at 308 nm wavelength. The substrate to be patterned was prepared by electron beam evaporation of 200 nm thick of the desired metal (Al, Ni, Au, Cu) with 5 nm thick Cr adhesion layer (the melting point of Cr is higher than the four metals studied here). The quartz mold was cut into a number of 1 mm$^2$ quartz pieces, which is smaller than the 2.5 × 2.5 mm$^2$ excimer laser spot size in order to ensure that the entire substrate area below the mold gets melted during the LADI process.

Excimer lasers are almost ideal sources for laser micro- or nano-patterning, some types of surface modifications, and thin film deposition. This is because they have high photon energies (short wavelengths), short pulse lengths (typically 10 to 40 ns), and relatively poor coherence (since an excimer laser's output is highly multimode and contains as many as $10^5$ transverse modes (Bäuerle 2000)). The high photon energy of an excimer laser allows for strong optical absorption in many metals and virtually all semiconductors. The short pulse length is a prerequisite for spatially well-defined surface heating (as $\delta\propto\sqrt{t_p}$) with negligible heating or damage of the bulk substrate (see next paragraph). In addition, the short pulse produces chemically stoichiometric ablation, which is one of the key advantages for pulsed laser deposition. Finally, the poor spatial coherence of excimer-laser light diminishes interference effects. Their disadvantages include low efficiency, poor pulse-to-pulse stability (when set at 160 mJ, the output energy ranged from 140 to 180 mJ), and high operating cost.

It should be pointed out that the optimal pulse length depends on the specific application. When substrate heating is not a concern, a longer pulse is desirable for more uniform heating through the film thickness and less damage of the film surface; a longer melting time also allows larger features to be patterned. If only the surface layer needs to be melted or ablated, then a shorter pulse is favored to reduce threshold fluence and substrate heating.

All laser fluences given in this chapter are values *before* passing through the quartz window and cover. The actual laser fluences received by the films should be about 15% less due to the reflection at four quartz/air interfaces. In addition, most experiments used only one laser pulse.

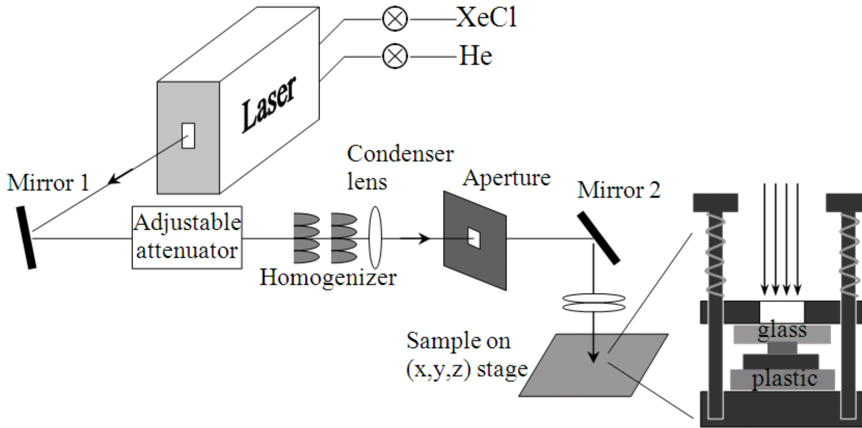


Fig. 6. Schematic setup of the excimer laser, optical components and sample stage. The laser can be used as light sources with different wavelengths by filling different rare-gas-halides into the laser gas chamber.

## 4. Applications of pulsed laser assisted nanofabrication

In this section we will present laser assisted direct imprint, wafer planarization, via-hole filling, transfer printing, and nano-tip formation.

### 4.1 Laser-assisted direct imprint (LADI)

The most straightforward application of laser assisted nanofabrication is LADI (Cui 2010, Chou 2002). In the LADI process, a single laser pulse passed through a transparent quartz mold and melted a thin layer of the substrate material, or the film material if it was different from the substrate. The characteristic time constant for electron-phonon collision to reach thermal equilibrium between excited electron gas and the lattice in metals is on the order of picoseconds, which is negligible compared to the laser pulse duration. The molten layer was then embossed by the quartz mold. Once the liquid layer re-solidified, the mold was separated from the substrate. As can be seen, the most prominent feature of LADI is that it is a one-step patterning process – it replaces the steps of resist patterning in photolithography or nanoimprint lithography, subsequent pattern transfer by etching or liftoff, and resist removal all into one single step. Besides LADI of metal or silicon, one can also imprint a polymer resist that absorbs UV light thus gets heated by the laser pulse (Xia 2003, Xia 2010).
Fig. 7 shows SEM images of 200 nm period Al, Au, Cu and Ni gratings with ~100 nm line-width imprinted by LADI. Only one pulse was used to melt and imprint those metals at a fluence of 0.22, 0.53, 0.24 and 0.41 J/cm$^2$ for Al, Au, Cu and Ni, respectively. We found that multiple pulses up to 50 pulses had insignificant effects to the imprint results. As shown in the figure, although 100 nm features in metal were imprinted, the resolution was not near

the sub-10 nm level as had been achieved in LADI of crystalline silicon (see below). This is partially due to two factors: (1) silicon expands 8.6% when re-solidified, which would help to press the un-solidified silicon to fill the void near the sharp corners; whereas Al, Au, Cu and Ni shrink 11 - 12% during re-solidification, which draws the un-solidified metals back from the sharp corners and thus results in an unfilled corner and rounded profile; and (2) the surface tension of molten silicon (0.78 N/m at its melting point) is lower than molten metals, so it is easier to imprint. We believe that here the volume shrinkage plays a major role, due to which the trench cannot be fully filled no matter how high a pressure is applied to overcome the surface tension. Besides front-side irradiation (laser beam passes from the mold to the substrate), metal can also be patterned by laser irradiation from the substrate side if the metal is deposited on a transparent substrate with a film thickness low enough (e.g. <300 nm) to be melted entirely.

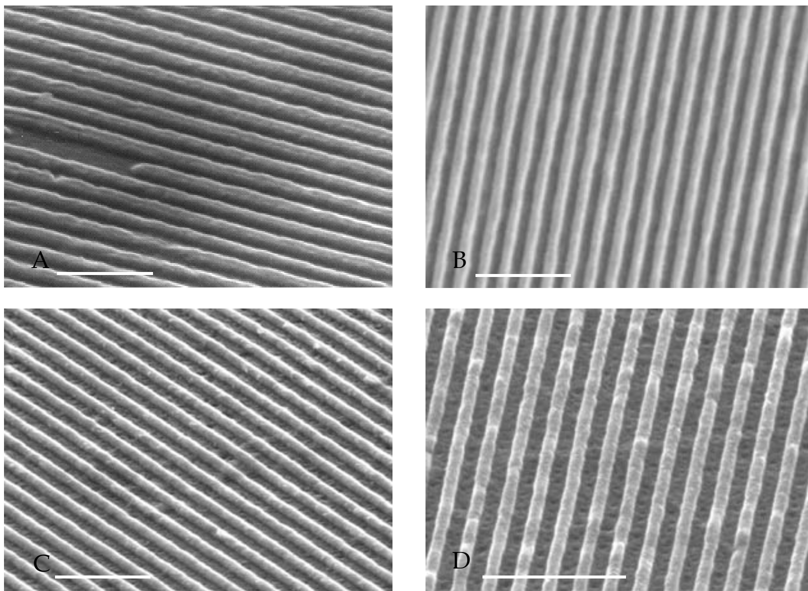


Fig. 7. SEM images of 200 nm-period metal gratings patterned by LADI. (A) Al, laser fluence 0.22 J/cm$^2$; (B) Au, 0.53 J/cm$^2$; (C) Cu, 0.24 J/cm$^2$; and (D) Ni, 0.41 J/cm$^2$. Scale bar is 1 μm.

We have also attempted to imprint tungsten. We found that it could be melted readily by a single laser pulse, but it could not be patterned with well defined gratings (yet grating pattern was still noticeable) using a quartz mold. This is likely because: (1) tungsten's melting point is 1800 K higher than that of quartz, hence quartz will be melted (softened) during LADI of W; (2) molten tungsten's surface tension is relatively high, nearly twice that of Cu, thus more difficult to imprint; (3) solid tungsten has a high Young's modulus E, three times that of Cu, leading to >3× higher thermal stress (equal to $E(\Delta L/L)$, with $\Delta L/L$ being thermal expansion between room temperature and melting point). Because of the high thermal stress, W film was found to crack after the LADI process.

LADI of single crystal silicon wafer (not thin film) is shown in Fig. 8. Due to the thermal expansion upon re-solidification that helps fill the sharp corners of the mold pattern, 10 nm

fine features on the mold were faithfully duplicated into the silicon. Reflection measurement, as shown in Fig. 8c, indicates that the silicon remained in liquid state for about 220 ns, roughly 10 times the pulse duration.

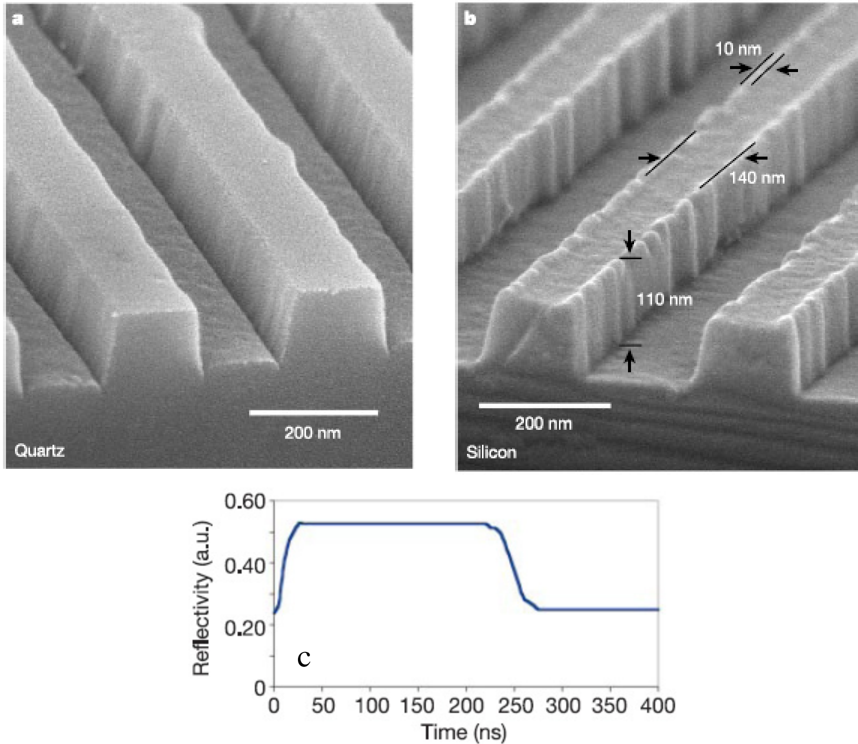


Fig. 8. LADI of single crystal silicon wafer. (a ) Quartz mold. The ~10 nm wide notches were caused by the reactive ion etching trenching effect during mold fabrication; (b) Imprinted pattern in silicon showing the notches were faithfully duplicated; (c) The reflectivity of a HeNe laser beam from the silicon surface versus the time, when the silicon surface is irradiated by a single laser pulse with 1.6 J/cm$^2$ fluence and 20 ns pulse duration. Molten Si, becoming a metal, gives a higher reflectivity.

#### 4.2 Laser-assisted wafer planarization

High-performance large-scale integrated circuits (ICs) require several levels of interconnect. Planarization processes which smooth and flatten the surface of an IC at various stages of fabrication are essential for high-resolution photolithography. Besides being smooth and flat, good film step-coverage without internal voids is also crucial for interconnection. Present IC interconnects are fabricated by the damascene process that consists of four major steps: patterning trenches in low-k dielectric materials by photolithography, sputtering metal plating base, copper electrical plating to fill the trench, and chemical mechanical polishing that planarizes the surface. The step-coverage of electrodeposited metal film, though better than other PVD (physical vapor deposition,

including evaporation and sputtering) metal films, is not as good as CVD (chemical vapor deposition) films because trench edges plate faster than trench bottoms. This problem will become even more severe for future ICs with narrower line-widths. Therefore, it is desirable to develop a technique that can both flatten the surface and enhance the step-coverage at the same time. Laser-assisted planarization might be one answer.

The setup for planarization is the same as LADI except that now a flat un-patterned quartz "mold" is used. The process is shown in Fig. 9. First, an insulator layer, typically thermal oxide which is also a good heat insulator, was patterned by NIL and RIE. Metal was then evaporated or sputtered onto the pattern. Finally, the metal was melted by a pulsed excimer laser and thus conformed to the flat and smooth surface of the quartz mold. IC interconnect typically consists of metal lines embedded in an insulator, which can be readily achieved here by etching away the metal on top using argon ion beam etching (IBE).

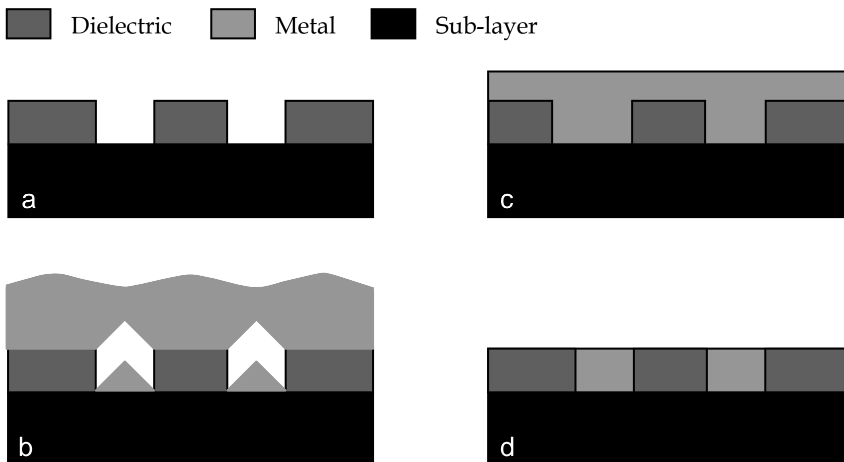


Fig. 9. Laser-assisted planarization. (a) Pattern insulator; (b) Deposit metal, here by evaporation; (c) Laser-melt and planarize. Metal on top of insulator was etched away by ion beam etching in (d).

Fig. 10 shows laser-assisted planarization of 180 nm-thick Cu evaporated onto a 200 nm-period $SiO_2$ grating on a silicon wafer. The laser fluence was 0.22 $J/cm^2$, which was close to the fluence used for LADI of Cu. As seen in Fig. 10(a), the step-coverage of evaporated Cu film was very poor. But after planarization the underlying voids were all filled with Cu (Fig. 10(b)), and the surface became very smooth with fluctuation less than 4 nm (Fig. 10(c)). Fig. 10(d) shows a 200 nm-period Cu grating embedded in an insulator (here silicon dioxide) fabricated by laser-assisted planarization and IBE removal of the Cu on top of the insulator. The laser fluence used for this sample was 70% higher than previous one, and the number of applied pulses was 150! Yet no apparent damage of Cu was found, suggesting that the number of pulses has only minor impact on laser-assisted planarization.

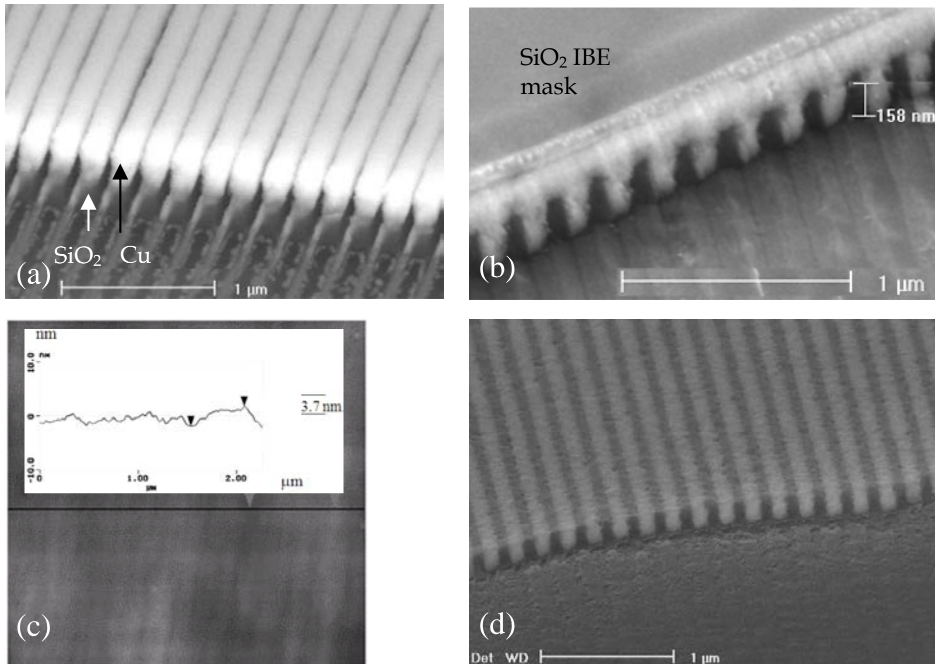


Fig. 10. Laser-assisted planarization of a 200 nm-period Cu grating on $SiO_2$. (a) Before planarization. (b) After planarization by 0.22 J/cm$^2$, shown here was a SEM image with evaporated $SiO_2$ IBE-mask still on top. (c) AFM image showing surface smoothness better than 4 nm. (d) Cu lines embedded in $SiO_2$ with flat surface fabricated after IBE removal of the Cu on top. (SEM cross-section was "cut" by IBE using evaporated $SiO_2$ as mask)

#### 4.3 Laser-assisted via-hole filling

Filling via holes or trenches with a deposited material is an important step in IC manufacturing. At present, the metal interconnect for ICs is typically fabricated by the dual damascene and, for the first wiring level, tungsten CVD plug process, where the via holes and trenches are etched in a dielectric material and subsequently filled up with a metal. Clearly, any voids left in the vias or trenches caused by poor step coverage will create a serious problem for the interconnect. Though superior to PVD, the step coverage of tungsten CVD is still limited by the low volatility of the precursor gas $WF_6$ that leads to a low vapor pressure. The result is a mass transport limited deposition rate, and the hole opening receives faster deposition and would be closed before the holes are completely filled. Another disadvantage of CVD is its relatively high thermal budget.

Atomic layer deposition (ALD) can achieve excellent step coverage in certain conditions. It is a modified form of CVD with gas precursors introduced one at a time with pump/purge in between. So the film is deposited one atomic layer per cycle, with a typical deposition rate of order 0.5 nm/min. Not only the slow deposition rate is a manufacturing issue, but also in ALD, voids will be formed if the via holes or trenches have a sidewall with negative angle.

The process we developed to fill via-holes is very close to the laser-assisted wafer planarization process, except that the trenches were replaced with deep and high aspect

ratio holes (Cui 2006). We fabricated in Si a hole array having 100 nm diameter, 500 nm depth (aspect ratio 5) and 200 nm inter-hole spacing (pitch). The hole array was patterned by nanoimprint lithography and etched by $Cl_2$/Ar RIE. As silicon is a good heat sink, a 15 nm thermal oxide layer was grown to reduce heat loss to the surrounding bulk Si, and to shrink the hole size at the same time. Finally, 200 nm Si or Cu was deposited on top of the hole array by e-beam evaporation. As expected and shown in Fig. 11a, evaporation has very poor step coverage, so the holes were only partially filled, with the sidewall of the holes receiving little deposition before the hole opening was closed. Fig. 11b shows via filling by Si, indicating a complete filling without voids. For via filling by Cu (Fig. 11c), the Cu plugs were found broken after wafer cut, and it is possible that the built-in stress caused by fast cooling of the liquid Cu has contributed to the Cu plug fracture. Nonetheless, we believe that most holes were completely filled to the bottom, as indicated by the Cu plug sections found on the bottom of the holes.

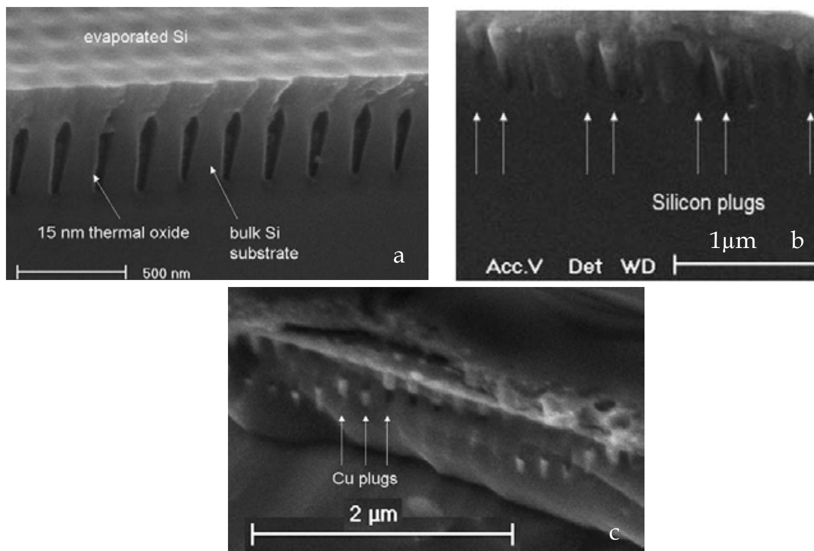


Fig. 11. (a) Holy array with 200 nm period and aspect ratio 5:1 after evaporation of filling material, here 200 nm Si. (15 nm thermal oxide has been grown to reduce heat loss to bulk Si). (b) Laser-assisted via-hole filling by α-Si, showing all holes were completely filled without void. (c) Laser-assisted via-hole filling by Cu.

#### 4.4 Laser-assisted nanotransfer printing

Laser-assisted nanotransfer printing (LA-nTP) is a dry-contact printing process which combines into one single step several steps needed for metal nanopatterning (Le Drogoff 2006). This process shares some attributes with laser-induced forward transfer (LIFT) process (Bohandy 1986). In LIFT, a thin laser-light absorbing film is irradiated with a focused laser pulse through a transparent support, and transferred, in the form of micron-sized dots, onto a suitable substrate facing it. The pattern is created through selective deposition on the substrate by scanning the laser beam. The resolution is hence determined and limited by the laser beam size and by the gap between the two samples (which determines the lateral spreading). In the

LA-nTP process, we use a pre-patterned transparent support in intimate contact with a substrate, therefore the resolution is no longer limited by the processing parameters but is determined only by the initial feature size on the transparent support.
The LA-nTP process is shown in Fig. 12. For proof of concept, we fabricated the donor support (DS) consisting a square chromium nanodot array with 200 nm period and 35 nm height (Fig. 12A). In parallel, we fabricated the acceptor substrate (AS) by photolithography and reactive ion etching, which contained an array of microwells with a diameter of 100 μm and depth 40 nm. The two patterned surfaces were then brought into contact by sandwiching them between two press plates. After shining with a laser pulse of fluence ~0.35 J/cm$^2$, the Cr nanodots were transferred only onto the protruded parts of the acceptor substrate that were in intimate contact with the donor support (Fig. 12C). We also found that using higher fluences (>0.6 J/cm$^2$), the results obtained were similar to those observed in other LIFT studies, namely Cr dot was transferred to the protruded areas as well as the recessed areas of the acceptor substrate with an increasing amount of spatter. At even higher fluencies (>1 J/cm$^2$), significant chromium vaporization was observed. On the other hand, experiments using laser fluencies lower than 0.2 J/cm$^2$ (below the melting threshold of a 30 nm Cr thin film) failed to transfer the Cr nanopatterns.

### 4.5 Laser-assisted nanotip formation

Nanotips have many applications such as scanning probe microscopy (SPM) and vacuum microelectronic devices like field emission display (FED), where their performance is often limited by the tip. Carbon nanotubes (Nguyen 2005, Jeong 2006) or nanocones (Chen 2006) have been studied extensively for applications as tips or emitters owning to its fine diameter and high aspect ratio. Silicon tips with high aspect ratio can be readily fabricated by highly anisotropic dry etching (Rangelow 2001). Metal is highly conductive and mechanically strong and robust, which are favorable properties for field emitter or scanning probe. Unfortunately, it is more challenging to fabricate metal tips on a wafer due to the difficulty in etching metals. Single metal tip can be routinely fabricated by focused ion beam milling or electrochemical etching (Kim 2006). But for FED or high throughput nanolithography using SPM, tip arrays are essential, which are very difficult to fabricate by the previous two methods. Metal tip arrays with low aspect ratio were traditionally fabricated by the Spindt process where the metal is evaporated through apertures that become gradually closed by the evaporated material (Spindt 1968). Similarly yet via a different mechanism, Au tips were formed by evaporation into porous alumina (Losic 2005). Alternatively, metal tips can be replicated by physical vapor deposition or electroplating into etch holes.
We found that sharp metal tips could also be self-formed by simply melting momentarily (~100 ns) a metal film deposited on a wafer with a second wafer placed a gap (submicrometers) below, as shown in Fig. 13 (Cui 2008). In the experiment, a silicon wafer with 500 nm thermal oxide was placed below the Cr film with a gap formed by a spacer. Next, a single excimer laser pulse (fluence 0.4 J/cm$^2$) shone through the quartz to melt the metal film momentarily that caused it to transfer toward the lower wafer. The two wafers were separated after Cr solidification and examined by SEM that showed nano-tip formation on both surfaces. The size, shape and location of the tips were random, but more regular tips are expected if the Cr is pre-patterned into identical isolated mesas. In addition, The ends of most tips resemble a sharp cone (not flat), hence they should be broken by the tensile force due to surface tension and/or volume shrinkage upon solidification; whereas those with a flat end were broken by mechanical force when the two wafers were separated.

The quartz and $SiO_2$ surface was found to be rather flat after the process. Since the melting temperature of quartz is much lower than the boiling temperature of Cr, a top $SiO_2$ layer of order 100 nm on both wafers should have been melted by heat transfer. However, due to the six orders higher viscosity of molten $SiO_2$ compared to that of chromium ($3.0 \times 10^6$ cP for $SiO_2$ versus 3.7 cP for Cr at 2673 K (Yaws 1998)), the flow of the molten $SiO_2$ is negligible, leading to no apparent distortion of the two wafer surfaces.

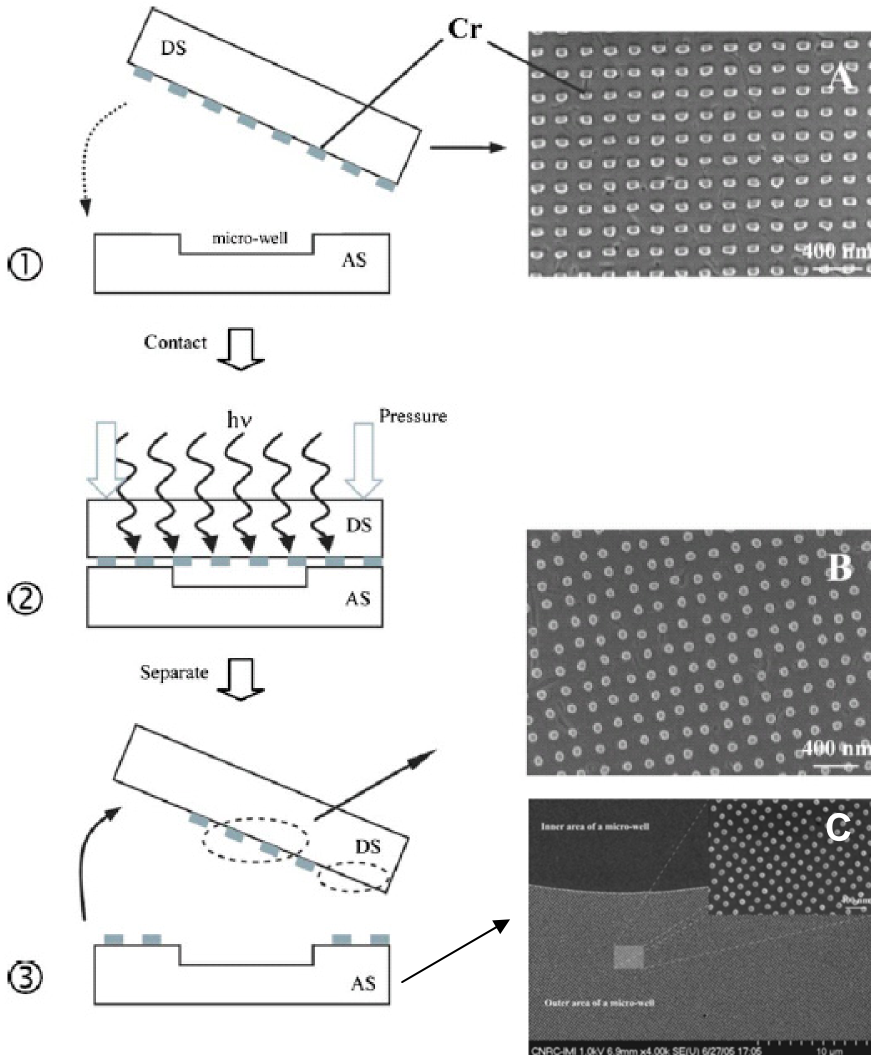


Fig. 12. (left) Schematic sequence of the fabrication process of LA-nTP (DS: donor support, AS: acceptor substrate). (right) A). Cr dot array on DS; B). Cr dot array on DS facing the recessed area of the AS; C). AS after LA-nTP showing Cr dot array was transferred from DS only to the protruded area of AS.

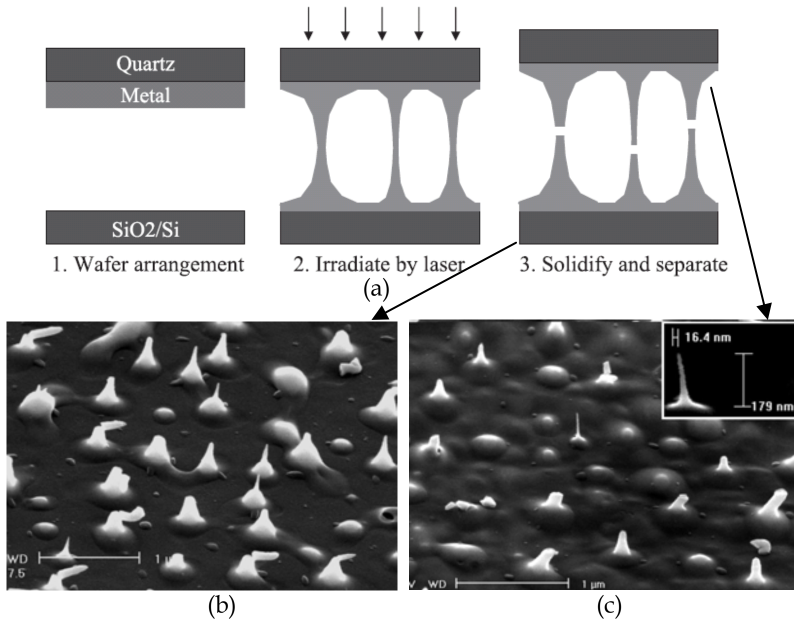


Fig. 13. (a) Schematic laser-induced metal nanotip formation process, with the metal here as 25 nm Cr. (b) Cr tips formed on the $Si/SiO_2$ substrate. (c) Cr tips formed on the quartz wafer. The inset is the zoom-in image of the tip at the center that has an apex of 10 nm and height of 180 nm. (This tip appears tilted due to SEM stage drift during imaging.)

The experimentally observed metal nano-tip formation phenomenon can be explained in term of an electro-hydrodynamic instability process as shown in Fig. 14. Briefly, the nano-tip formation can be roughly divided into four stages: free charge buildup, mass transfer to the lower wafer upon laser illumination, liquid pillar formation due to electrostatic attraction, and solidification and break of the pillars.
When the two wafers are brought close together, free charges are built up on both wafers due to the work function difference between Cr and $SiO_2$, which results in a strong electric field of order $10^5$ V/cm for a 500 nm gap. Interaction between electric field and induced dipole or free charges accumulated at the interface results in an electrostatic pressure. The attractive electrostatic force sets the two molten metal films into tension subject to infinitesimal disturbances, and interfacial ripples start to develop. The periodicity of the ripple that determines the areal number density of the tips would depend on the liquid metal density, film thickness, surface tension and work function difference. The electrostatic force between two approaching peaks is further enhanced due to the locally strengthened electric field. As a result, the electrostatic force keeps on overcoming the stabilizing surface tension and viscous force and pulling the peaks further together until the peaks are bridged together to form a liquid bridge or the liquid metal solidifies. Once the peaks bridged together, the charges are neutralized and thus the electrostatic force disappears, and the bridges may break by the large surface tension of liquid metal that is about 20 times that of water. Meanwhile, solidification propagates from the two metal-wafer interfaces toward the gap center, because the wafers are heat sinks and the temperature distribution before

solidification across the gap should be uniform (since the melting time is order 100 ns that is much longer than pulse duration). Nano-tips are formed at the broken bridge necks before or during solidification due to surface tension and volume shrinkage, or after the two wafers were separated.

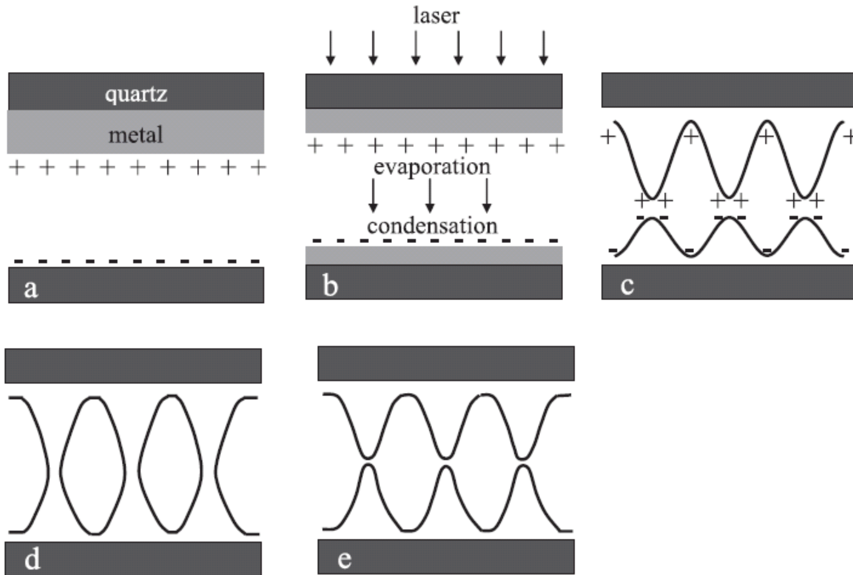


Fig. 14. Schematic of the physical mechanism behind the nano-tip formation. (a) Build-up of free charges on the two wafers. (b) Metal transfer to lower wafer by evaporation-condensation. (c) Nano-bridge formation due to attractive electrostatic force. (d) Bridging of approaching peaks and charge neutralization. (e) Break of bridges upon solidification or after separation.

## 5. Lower and upper limit of achievable feature size

So far, only structures with feature size of about 100 nm were described. Laser-assisted processes for much smaller and larger feature sizes will be discussed in this section, with a focus on factors that limit the achievable feature sizes of the techniques.

### 5.1 Resolution limit

In LADI, planarization, and via-hole filling processes, squeezing liquid metals or semiconductors into small trenches or via holes will be ultimately limited by the pulling pressure due to surface tension. Fig. 15 shows schematic drawing illustrating how much pressure is needed to fill trenches or via holes. For all cases, the pulling pressure is proportional to the surface tension constant $\gamma$ and inversely proportional to feature size. Therefore, there is no fundamental resolution limit provided the applied pressure is high enough. In practice, the liquid metal and silicon generally have surface tension $\gamma$ on the order of 1 N/m (for water, it is 0.076 N/m), which leads to a pressure of 200 bar to fill in 100 nm-wide trenches, or 2000 bar for 10 nm-wide trenches. This pressure is considerably higher

than that used for regular thermal nanoimprint lithography (order of 10 bar). However, considerably lower applied pressure would be sufficient for patterning metals and silicon if: (1) the molten metal partly wets the $SiO_2$ substrate; and/or (2) the mold consists of sparse protruded patterns to create sparse recessed metal features (such as a periodic hole array having diameter ~100 nm and pitch 500–600 nm in Au for extraordinary optical transmission devices (Lesuffleur 2008)), because the effective local pressure at the protruded mold features is significantly higher than the applied pressure (applied force divided by wafer surface area).

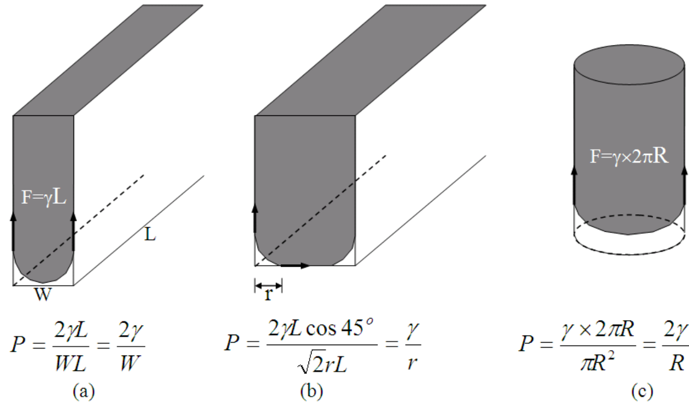


Fig. 15. Schematic drawing showing the calculation of minimum pressure to squeeze a liquid into (a) a trench, (b) a trench with liquid partly squeezed against the bottom, and (c) a via hole. The pressures are calculated assuming $90^o$ contact angle and no wetting/adhesion.

### 5.2 Upper limit of achievable feature size

The maximum feature size that can be patterned depends on how far the molten metal can flow before re-solidification. For a rough estimation, the dynamic flowing process is modeled as in Fig. 16. It is assumed that the grating structure has a period 2L and a trench depth $h_0$; and the entire layer is melted at t=0 and re-solidification takes place simultaneously throughout the film thickness at time t=τ. The mold will travel a distance of $h_0/2$ and the residual molten layer thickness will decrease to $h_0/2$ when the trench is fully filled. Since L is large, the effect of surface tension can be ignored and thus the internal pressure at x=L/2 is zero. There are three forces acting on the liquid: the pressing force from the mold, the viscous force, and the inertial force.

We first consider only the effect of viscous force by assuming that a steady flow develops momentarily at t=0 (i.e. ignore inertial force). Then the maximum grating half pitch $L_1$ that can be patterned (trench fully filled) before the liquid metal solidifies is given by (Heyderman 2000, Cui 2006):

$$L_1 = h\sqrt{\frac{P\tau}{\mu}} \tag{11}$$

where $h$ is the metal film thickness (200 nm), P is the applied pressure (order 100 bar), μ is the viscosity, and τ is the melting duration (~ 200 ns) that depends on laser fluence. The

viscosity of molten Au and Cu is around 4 cp (only ~5× that of wafer (Yaws 1998)), leading to $L_1$~ 5 μm. To pattern isolated metal mesas, the liquid flows from four sides to fill a square-shaped hole in the mold, so the maximum patternable mesa size should be roughly doubled to ~10 μm, which qualitatively agrees with the experiment (17 μm). Moreover, it is interesting to see how far molten $SiO_2$ can flow under similar conditions. For example, its viscosity at 2200 K is $8\times10^7$ cp (a very tacky "liquid"), 7 orders higher than that of Au and Cu, leading to a calculated $L_1$ of only ~1 nm if assuming a top 200 nm $SiO_2$ layer is molten. This explains why the quartz mold can be used to pattern a metal at temperature slightly higher than its melting point, though the mold could not be used repeatedly for >>10 times.

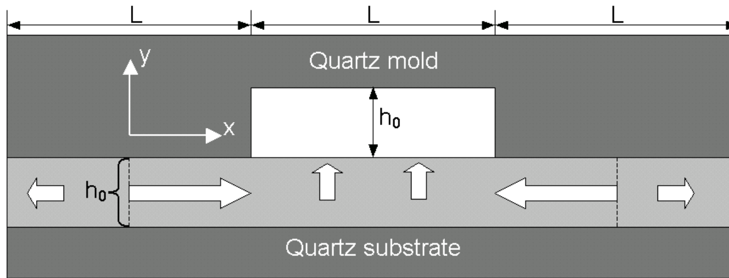


Fig. 16. Dynamics of molten metal flowing into trenches during LADI. Assume that grating line-width and trench-width are both equal to L, and trench depth and molten layer thickness are both equal to $h_0$.

Next, to estimate the inertial force which decides how fast the steady flow develops, it is assumed that the liquid metal is inviscid (μ = 0) for simplicity. The applied pressure is to accelerate the flow along the x-direction with acceleration given by (note that the effective pressure is doubled for a grating with equal line and trench width, and z is the direction perpendicular to the paper):

$$a = \frac{F}{m} = \frac{2P \times hz}{\rho \times hz(L/2)} = \frac{4P}{\rho L} \tag{12}$$

The velocity is then u=at at time t, and the flow-rate Q=uh=ath (ignoring the z-dimension). On the other hand, the volume of the liquid changes at a rate

$$Q = -\frac{L}{2}\frac{dh}{dt} \tag{13}$$

Therefore, solving the equation

$$\frac{4P}{\rho L} th = -\frac{L}{2}\frac{dh}{dt} \tag{14}$$

gives ($h=h_0$, $h_0/2$ at $t=0$, $\tau$)

$$L_2 = 2\sqrt{\frac{P}{\rho \ln 2}}\tau \sim \sqrt{\frac{P}{\rho}}\tau \tag{15}$$

Thus even within a very short melting time of order 100 ns, the calculated $L_2$ values are order 20 μm for applied pressure of 100 bar.

The critical length can also be estimated by experiment. For example, Fig. 17a shows a backside-irradiated 200 nm-thick Ni film by a single laser pulse with fluence 0.60 J/cm$^2$ that partly blew the film off the substrate. The surface tension was the force driving the flow, and the driving pressure can be estimated by $2\gamma/h$ (h is the film thickness, and the factor 2 accounts for the top and bottom surface/interface), which was 180 bar. The SEM image indicates that Ni flowed about 4 μm before the film re-solidified. For LADI, we achieved 17 μm isolated Cu mesas with 100 nm height (Fig. 17b), but it was found that a pattern of several tens of micrometer size required multiple pulses. Therefore, the maximum patternable feature size using one laser pulse lies on the lower tens of μm, close to the theoretical prediction.

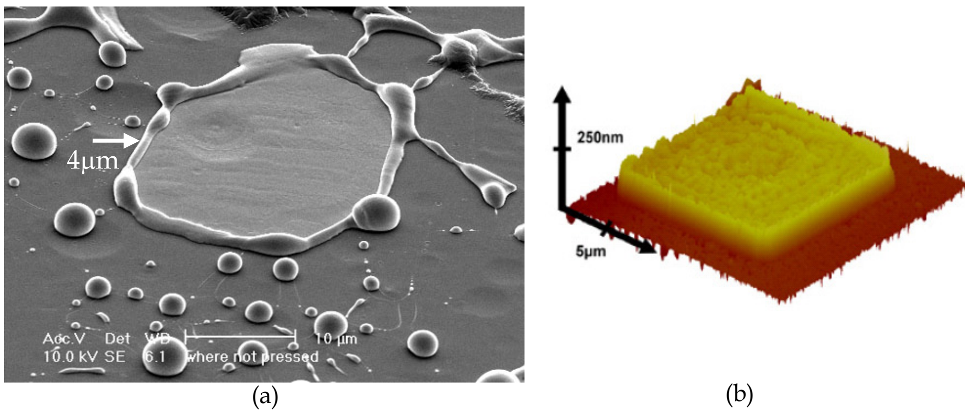


Fig. 17. (a) A 200 nm-thick Ni film irradiated from backside by a single laser pulse with a fluence of 0.60 J/cm$^2$ that partly blew the film off the substrate. The liquid traveled about 4 μm before it froze. (b) AFM image of isolated Cu mesas patterned by LADI at laser fluence of 0.45 J /cm$^2$. The mesas have a length on each side of 17 μm and a height of 100 nm.

## 6. Conclusion

In this chapter, five nanofabrication processes using pulsed excimer laser were described. These methods share the common advantage of being orders faster than most other fabrication techniques. They are also very suitable to patterning metals, which are more difficult to process than semiconductors by conventional lithographies and etching.

The first was laser-assisted direct imprinting, which produced 200 nm-period Cu, Ni and Al gratings over about 1 mm$^2$ area within ~100 ns. LADI of W failed due to its high thermal stress. The second was wafer planarization using a flat and smooth "mold". With this technique, Cu surface was planarized by laser melting under pressure, which also squeezed the molten film to fill completely voids under the film. Cu conducting lines embedded in a dielectric matrix were created by an additional etching step. Third, a similar process could also fill 100 nm-wide and 500 nm-deep via-holes with Si and Cu. Fourth, sub-100 nm diameter Cr dots were melt-transferred to the receiving substrate using a laser-induced

nanotransfer printing. Fifth, Cr tips with apex diameter as small as 10 nm and aspect ratio up to 10:1 were achieved by laser melting and boiling through the proposed mechanism of an electro-hydrodynamic instability. Such tips could be employed as field emitters for flat panel display, or as tips for scanning probe microscopy.

For laser-assisted direct imprint, planarization, and via-hole filling, the resolution is determined by the balance between the surface tension and the applied pressure. Whereas the maximum patternable feature size is limited by the liquid viscosity and friction at the interfaces. Strong adhesion between the mold and the molten material rules out clean separation thus sets another constraint on processable materials. To scale up the process to full wafer patterning, the challenge is the availability of pulsed laser with large enough beam size and the very high pressure normally needed.

## 7. Acknowledgment

I would like to thank my PhD supervisor at Princeton University, Professor Stephen Y Chou, under whose guidance I carried out most of the research presented in this chapter.

## 8. References

Allmen, M. & Blatter, A. (1995). Laser-beam Interactions with Materials – Physical Principles and Applications, 2ed edition, Springer series in materials science.

Austin, M. D.; Ge, H.; Wu, W.; Li, M.; Yu, Z.; Wasserman, D.; Lyon, S. A. & Chou, S. Y. (2004). Fabrication of 5 nm linewidth and 14 nm pitch features by nanoimprint lithography. *Appl. Phys. Lett.* 84, 5299–301.

Baeri, P.; Campisano, S. U.; Foti, G. & Rimini, E. (1979). Melting model for pulsing-laser annealing of implanted semiconductors. *Journal of Applied Physics*, 50, 788.

Bäuerle, D. (2000). Laser Processing and Chemistry. 3rd edition, Springer-Verlag.

Bohandy, J.; Kim, B. F. & Adrian F. J. (1986). Metal deposition from a supported metal film using an excimer laser. *J. Appl. Phys.* 60, 1538.

Boulmer-Leborgne (1995). Laser-material interaction, plasma formation and applications, in Applications of Particle and Laser Beams in Materials Technology, NATO ASI Series E: Applied Sciences, Volume 283.

Buzzi, S.; Robin, F.; Callegari, V. & Loffler, J. F. (2008). Metal direct nanoimprinting for photonics. *Microelectron. Eng.* 85, 419-424.

Chen, H. L.; Chuang, S. Y.; Cheng, H. C.; Lin, C. H. & Chu, T. C. (2006). Directly patterning metal films by nanoimprint lithography with low-temperature and low-pressure. *Microelectron. Eng.* 83, 893-896.

Chen, I. C.; Chen, L. H.; Ye, X. R.; Daraio, C.; Jin, S.; Orme, C. A.; Quist, A. & Lal, R. (2006). Extremely sharp carbon nanocone probes for atomic force microscopy imaging. *Appl. Phys. Lett.* 88, 153102.

Chou, S. Y.; Krauss, P. R. & Renstrom, P. J. (1996). Imprint Lithography with 25-Nanometer Resolution. *Science*, 272, 85–7.

Chou, S. Y.; Keimel, C. & Gu, J. (2002). Ultrafast and direct imprint of nanostructures in silicon. *Nature*, 417, 835–837.

Chou, S. Y. & Xia Q. F. (2008). Improved nanofabrication through guided transient liquefaction. *Nature Nanotechnology*, 3(5), 295-300.

Chrisey, D. B. & Hubler, G. K. (editor) (1994). Pulsed Laser Deposition of Thin Films. Wiley-Interscience.

Chuang, S. Y.; Chen, H. L.; Kuo, S. S.; Lai, Y. H. & Lee, C. C. (2008). Using direct nanoimprinting to study extraordinary transmission in textured metal films. *Opt. Express*, 16(4), 2415-2422.

Cui, B. & Veres, T. (2006). Pattern replication of 100 nm to millimeter-scale features by thermal nanoimprint lithography. *Microelectron. Eng.* 83, 902-905.

Cui, B.; Wu, W.; Keimel, C. & Chou, S. Y. (2006). Filling of Via Holes by Laser-Assisted Direct Imprint (LADI). *Microelectron. Eng.*, 83(4-9), 1547-1550.

Cui, B.; Wu, L. & Chou, S. Y. (2008). Fabrication of high aspect ratio metal nano-tips by nanosecond pulse laser melting. *Nanotechnol.* 19, 345303.

Cui, B.; Keimel, C. & Chou, S. Y. (2010). Ultrafast Direct Imprint of Nanostructures in Metals by Pulsed Laser Melting. *Nanotechnol.* 21, 045303.

Heyderman, L. J.; Schift, H.; David, C.; Gobrecht, J. & Schweizer, T. (2000). Flow behaviour of thin polymer films used for hot embossing lithography. *Microelectron. Eng.* 54, 229-245.

Hirai, Y.; Ushiro, T.; Kanakugi, T. & Matsuura, T. (2003). *SPIE – Int. Soc. Opt. Eng.* 5220 74-81.

Hua, F.; Sun, Y.; Gaur, A.; Meitl, M. A.; Bilhaut, L.; Rotkina, L.; Wang, J.; Geil, P.; Shim, M. & Rogers, J. A. (2004). Polymer Imprint Lithography with Molecular-Scale Resolution. *Nano Lett.* 4, 2467–2471.

Hughes, T. P. (1975). Plasmas and Laser Light. Adam Hilger.

Jeong, T.; Heo, J.; Lee, J.; Park, S.; Jin, Y.; Kim, J. M.; Oh, T.; Park, C.; Yoo, J. B.;, Gong, B.; Lee, N. & Yu, S. (2006). Field emission from carbon nanotube emitters fabricated by the metal intermediation layer. *J. Appl. Phys.* 100, 064308.

Kim, C.; Burrows, P. E. & Forrest, S. R. (2000). Micropatterning of Organic Electronic Devices by Cold-Welding. *Science*, 288, 831–833.

Kim, P.; Kim, J. H.; Jeong, M. S.; Ko, D. K.; Lee, J. & Jeong, S. (2006). Efficient electrochemical etching method to fabricate sharp metallic tips for scanning probe microscopes. *Rev. Sci. Instrum.* 77, 103706.

Le Drogoff, B.; Cui, B. & Veres, T. (2006). Fast 3D Nanostructure Fabrication by Laser-Assisted nano-Transfer Printing. *Appl. Phys. Lett.*, 89, 113103.

Lesuffleur, A,; Im, H.; Lindquist, N. C.; Lim, K. S. & Oh, S. H. (2008). Laser-illuminated nanohole arrays for multiplex plasmonic microarray sensing. *Opt. Express,* 16, 219–24.

Losic, D.; Shapter, J. G.; Mitchell, J. G. & Voelcker, N. H. (2005). Fabrication of gold nanorod arrays by templating from porous alumina. *Nanotechnol.* 16, 2275

Nguyen, C. V.; Ye, Q. & Meyyappan, M. (2005). Carbon nanotube tips for scanning probe microscopy: fabrication and high aspect ratio nanometrology. *Meas. Sci. Technol.* 16, 2138.

Pang, S. W.; Tamamura, T.; Nakao, M.; Ozawa, A. & Masuda, H. (1998). Direct nano-printing on Al substrate using a SiC mold. *J. Vac. Sci. Technol. B*, 16, 1145–1149.

Poate, J. M. & Mayer, J. W. (editor) (1982). Laser Annealing of Semiconductors. Academic Press.

Rangelow, I. W. & Biehl, S. (2001). High aspect ratio silicon tips field emitter array. *Microelectron. Eng.* 57-58, 613.

Schift, H. (2008). Nanoimprint lithography: An old story in modern times? A review. *J. Vac. Sci. Technol. B*, 26 458–80.

Shank, C. V.; Yen, R. & Hirlimann, C. (1983). Time-resolved reflectivity measurements of femtosecond-optical-pulse induced phase-transitions in silicon. *Physical Review Letters*, 50(6), 454.

Spindt, C. A. (1968). J. Appl. Phys. 39 3504 A Thin-Film Field-Emission Cathode.

Xia, Q.; Keimel, K.; Ge, H.; Yu, Z.; Wu, W. & Chou, S. Y. (2003). Ultrafast patterning of nanostructures in polymers using laser assisted nanoimprint lithography. *Appl. Phys. Lett.* 83(21), 4417-4419.

Xia, Q.; Morton K. J.; Austin, R. H. & Chou, S. Y. (2008). Sub-10 nm Self-Enclosed Self-Limited Nanofluidic Channel Arrays, *Nano Lett.*, 8(11), 3830-3833.

Xia, Q. & Chou, S. Y. (2010). Applications of excimer laser in nanofabrication, *Appl Phys A* 98, 9–59.

Yaws, C. L. (1998). Chemical Properties Handbook: Physical, Thermodynamics, Environmental Transport, Safety & Health Related Properties for Organic & Inorganic Chemicals (McGraw-Hill Professional).

Yu, J. & Bulovic, V. (2007). Micropatterning metal electrode of organic light emitting devices using rapid polydimethylsiloxane lift-off. *Appl. Phys. Lett.* 91, 043102.